

See discussions, stats, and author profiles for this publication at: <https://www.researchgate.net/publication/270654510>

Plasmon Enhancement Effect in Au Gold Nanorods@Cu₂O Core–Shell Nanostructures and Their Use in Probing Defect States

ARTICLE in LANGMUIR · JANUARY 2015

Impact Factor: 4.46 · DOI: 10.1021/la503988e · Source: PubMed

CITATIONS

5

READS

55

10 AUTHORS, INCLUDING:



Xiaochun Wu

National Center for Nanoscience and Technol...

100 PUBLICATIONS 2,833 CITATIONS

SEE PROFILE



Wenqi Liu

Qingdao University

17 PUBLICATIONS 170 CITATIONS

SEE PROFILE



Tao Wen

Institute of Basic Medical Sciences, Chinese Ac...

24 PUBLICATIONS 298 CITATIONS

SEE PROFILE



Min Song

Central South University

148 PUBLICATIONS 918 CITATIONS

SEE PROFILE

Plasmon Enhancement Effect in Au Gold Nanorods@Cu₂O Core–Shell Nanostructures and Their Use in Probing Defect States

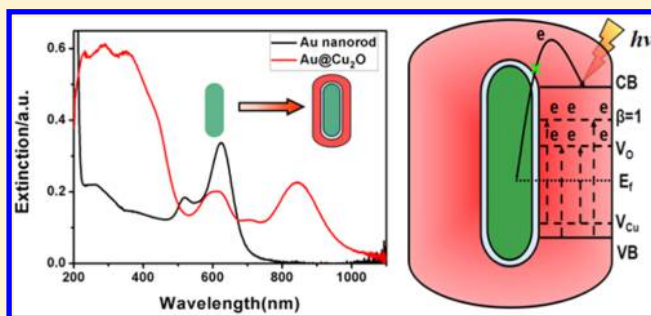
Xiaowei Shi,^{†,‡} Yinglu Ji,[‡] Shuai Hou,[‡] Wenqi Liu,[‡] Hui Zhang,[‡] Tao Wen,[‡] Jiao Yan,[‡] Min Song,^{*,†} Zhijian Hu,^{*,‡} and Xiaochun Wu^{*,‡}

[†]State Key Laboratory for Powder Metallurgy, Central South University, Changsha 410006, PR China

[‡]CAS Key Laboratory of Standardization and Measurement for Nanotechnology, National Center for Nanoscience and Technology, Beijing 100190, PR China

S Supporting Information

ABSTRACT: Au@Cu₂O core–shell nanostructures are fabricated to have a plasmon enhancement effect using Au nanorods (Au NRs) as a plasmon-tailorable core. By varying the concentration of Au NRs, we can tune the shell thickness in the range of 10–25 nm. The shell is composed of Cu₂O nanocrystallites. Because of the thin shells, the extinction spectra at wavelength >500 nm are dominated by the Au core. However, the large dielectric constant of the shell causes an obvious red shift of the surface plasmon resonance (SPR) band of the Au nanorod. Besides, transverse octupolar SPR appears as a result of the anisotropy of the core and the high dielectric constant of the shell. The anisotropic geometry of the Au NR is found to support the octupolar resonances at smaller sizes than for their spherical counterpart. Theoretical simulations indicate that the transverse SPR bands are divided into two resonances, which are dipolar- and octupolar-dominant, respectively. The Cu₂O shell degrades via a defect-mediated oxidative pathway, which is aggravated upon longitudinal SPR excitation. The SPR-mediated local field enhancement and resonance energy transfer are found to enhance the excitation of the defect states in the shell, thus providing a simple yet selective probing strategy for defect states.



INTRODUCTION

Photocatalysts can utilize solar energy to induce useful redox reactions and therefore are of considerable interest for solar energy conversion and environmental pollutant purification.¹ Many semiconductors, such as TiO₂ and ZnO, can act as photocatalysts.^{2,3} However, the wide band gap and fast recombination of the photogenerated electrons and holes decrease the photocatalytic efficiency and limit their applications. In well-known dye-sensitized solar cells (DSSCs), organic dyes have been used as photosensitizers to enable photocatalytic activities in the visible spectrum range.⁴ An instability, however, is concerned.⁵ Plasmonic nanoparticles, especially gold and silver, have strong localized surface plasmon resonance (SPR) in the visible spectrum range. Their SPR can be further tuned by varying the particle size, shape, and surrounding dielectric environments. Easily tunable SPR features and high stability make plasmonic nanostructures a new kind of robust wide-spectrum-response photosensitizer. Apart from light sensitization, localized SPR is found to endow photocatalysis with extra benefits. For instance, in metal@semiconductor core–shell structures, three main SPR enhanced effects have been observed to boost the photocatalysis efficiency greatly: (1) Direct electron transfer (DET) occurs between the plasmonic metal and the semiconductor when they are in direct contact.^{6,7} (2) Via an SPR-mediated local

electromagnetic field (LEMF), the absorbance coefficients of semiconductors can be effectively increased.^{8–10} (3) Via either radiative or nonradiative plasmon resonance energy transfer (RET), the number of photoinduced charge carries in the semiconductor can be increased.^{11,12} SPR-mediated radiative energy transfer requires the energy overlap of plasmon resonance with the band gap of the semiconductor. Non-radiative RET, in contrast, has been observed under both overlap and nonoverlap conditions.

Cu₂O is a p-type semiconductor with a band gap of 2.0–2.2 eV.¹³ Owing to the narrow band gap, Cu₂O can harvest solar energy in the visible spectrum region and thus has attracted a great amount of attention for solar-energy-driven applications such as low-cost photovoltaics, water splitting for H₂ generation, photocatalytic degradation of organic contaminants, and other energy-related applications.¹⁴ However, Cu₂O has a high refractive index (almost 2.7 at a wavelength longer than 600 nm),^{15,16} which makes the tailoring of the SPR features for neighboring plasmonic nanoparticles much easier.¹⁷ Au nanoparticles have drawn much attention because of their chemical stability, tunable SPR, and high electromagnetic field intensity.

Received: October 8, 2014

Revised: January 6, 2015

Published: January 7, 2015

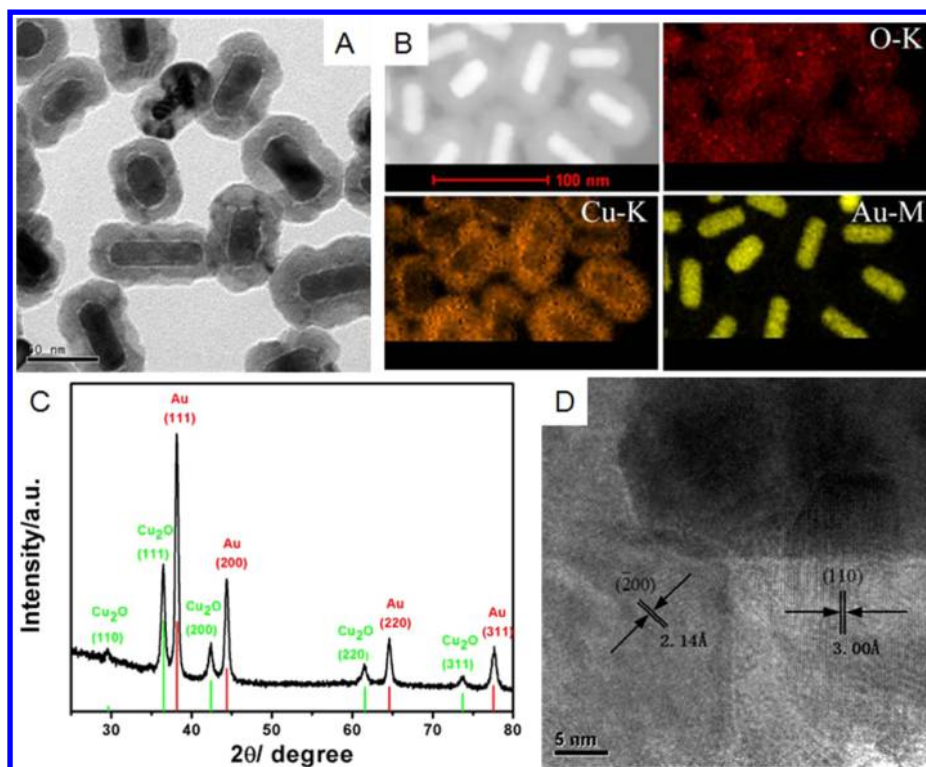


Figure 1. Characterization of Au@Cu₂O-4. (A) TEM image, (B) HAADF-STEM image and corresponding elemental mapping, (C) XRD pattern, and (D) HRTEM image.

These properties can enhance the photocatalysis capability effectively. Recently, Au@Cu₂O nanostructures with different shapes and sizes have been successfully synthesized by reducing cupric salts on Au cores under alkaline conditions.^{15–19} Mainly, Cu₂O exposed-facet-tailored photocatalytic activities have been studied.^{19,20} For instance, Wang et al. synthesized Au@Cu₂O nanoparticles with different exposed facets and showed that the {110} facets of Cu₂O are more photocatalytically active.²⁰ However, owing to relatively thick Cu₂O shells in most reported core–shell structures, the plasmonic effects of the Au core were not effectively utilized.^{18,19}

As mentioned above, to enhance the photocatalytic activity of semiconductors such as TiO₂ in the visible spectrum range, doping and creating defects within band gap have been attempted. Furthermore, plasmonic nanostructures have been integrated to enhance the photocatalytic capability in this region further because of the low state density. For instance, by adding Au NPs, Liu et al. observed an enhancement of up to 66-fold in the photocatalytic splitting of water by TiO₂ upon visible plasmon excitation.¹⁰ A defect-based spectrum extension could be a two-edged sword. Some defect states may accelerate the combination of photoinduced charge carriers and thus could play a negative role in photocatalysis. Therefore, developing useful ways to probe and differentiate various defects is critical to the eventual optimization of photocatalytic performance. Considering the wide tailoring ability of localized SPR in plasmonic nanoparticles, the activity of given defect states can be selectively enhanced by the excitation of specific SPR. It may provide a useful way to detect and distinguish the defect states.

We attempt herein to fabricate Au@Cu₂O with a thin shell thickness in order to explore the plasmonic effect of the Au core fully. Cu₂O is used as a shell material because of its defect-

mediated photodegradation. Au nanorods (Au NRs) are employed as the core because they provide a wide-range LSPR response below the band gap of bulk Cu₂O. Small Cu₂O nanoparticles are found to aggregate and fuse on the Au core. Eventually, a relatively uniform and compact Cu₂O shell is formed with a thin shell thickness (10–25 nm). The synthesized Au@Cu₂O structures preserve the shape of the Au nanorod. At the thin shell thickness, longitudinal surface plasmon resonance (LSPR) exhibits a large red shift as a result of the high dielectric constant of Cu₂O. In addition, we find an obviously broadened transverse SPR band. Theoretical simulations indicate that there exist two different transverse resonance bands, which are dipolar and octupolar dominant, respectively. The occurrence of octupolar resonances is caused by the high refractive index of Cu₂O and the anisotropic shape of the core. Besides, the calculated spectra show that Au@Cu₂O is a good photoabsorber and may find application in photothermal energy conversion. The LSPR band of the nanostructure is between 800 and 870 nm and is in resonance with the defect states within the band gap of Cu₂O. The defect-state-induced photodegradation of Cu₂O is enhanced upon LSPR excitation. The enhancement of defect-state excitation leads to increased photooxidation. In combination with the SERS results, SPR-mediated near-field enhancement and nonradiative resonance-energy transfer are responsible for the photodegradation.

RESULTS AND DISCUSSION

Structural Characterization of the Au@Cu₂O Samples.

Figure 1 shows the structural characterization of the as-obtained Au@Cu₂O core–shell nanoparticles. The TEM and elemental mapping images (Figure 1A,B) show clearly that the composite nanoparticle is a core–shell structure and that each

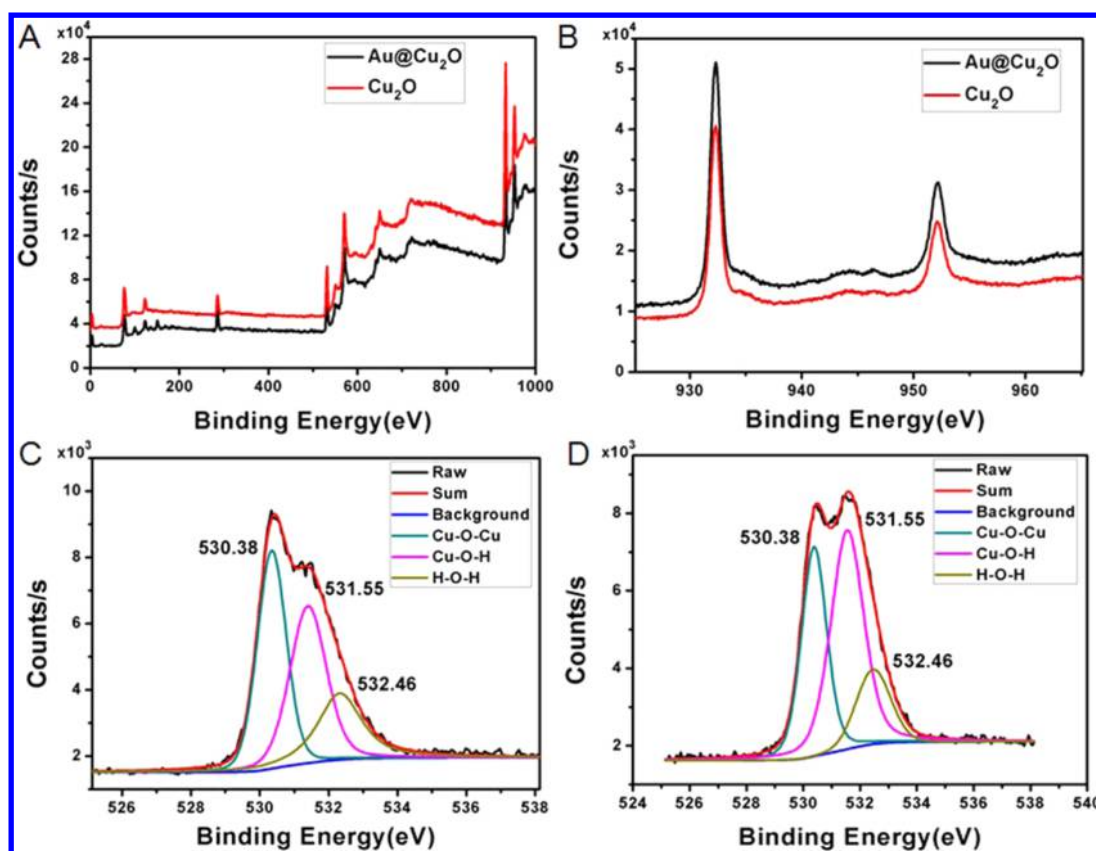


Figure 2. XPS spectra. (A) Survey spectra of Au@Cu₂O and Cu₂O, (B) Cu 2p, and (C) curve-fitting results of O 1s in Cu₂O and (D) in Au@Cu₂O.

core–shell structure has only one Au rod core. The core–shell structure exhibits rodlike morphology, preserving the shape of the Au core (Figure S1). Some nanostructures exhibit Moiré fringe patterns originating from mismatched crystalline lattices of Au and Cu₂O.^{20,21} Also, the TEM image shows that there is a narrow bright region between the core and the shell, which indicates that these locations may not directly contact each other. The XRD patterns in Figure 1C show that the structure is composed of Au (PDF 65-2870) and Cu₂O (PDF 77-0199). The HRTEM image in Figure 1D indicates that the Cu₂O shell is a polycrystalline structure and is composed of Cu₂O monocrystalline domains with different orientations. To check the compactness of the shell, the Cu/Au ratio from SEM EDX analysis and the TEM size calculation are compared. They indicate that the compactness of the shell is quite good. X-ray photoelectron spectroscopy (XPS) is used to determine the surface components of the shell. In Figure 2, the peak at 932.3 eV corresponds to Cu⁺ 2p_{2/3}, indicating the presence of Cu₂O.²² Two weak shakeup satellites at about 945.4 eV are typical characteristics of Cu²⁺ and indicate the existence of a small amount of Cu²⁺, possibly in the form of hydrated cupric hydroxide on the outer surface of the Cu₂O shell as shown in O 1s analysis. The O 1s band can be deconvoluted into three peaks, related to Cu₂O and hydrated cupric hydroxide, respectively.²³ The Cu/O atom ratios from XPS are 1:1.99 and 1:1.94 for Cu₂O and Au@Cu₂O-2, respectively. These values deviate greatly from 2:1 in Cu₂O, supporting the existence of surface copper hydroxides.

The amount of cetyltrimethylammonium bromide (CTAB) surfactant plays a unique role in assisting the aggregating of small Cu₂O NPs onto the Au core (Figure S2). At CTAB concentration lower than 10 mM, the final products contain a

large number of pure Cu₂O NPs (Figure S2A, red circle). When the CTAB concentration is increased to 33 mM and higher, the self-aggregation of Cu₂O is greatly suppressed (Figure S2B–D). We believe that aggregation of Cu₂O on the Au core and the self-aggregation of Cu₂O are competitive. Too low a CTAB concentration leads to a poor coating of small Cu₂O NPs. It favors their self-aggregation.

The growth rate of the Cu₂O shell is very fast. Just after 2 min, 84% of the shell has formed as seen from the extinction values at 400 nm (Ext_{400 nm}) and the LSPR shift. At 6 min, the formation of the shell is close to being finished (Figure 3A,B). Prolonged growth time leads to only small changes in the extinction spectra. Intermediates at 2, 6, and 25 min were checked with TEM. At 2 min, many small Cu₂O particles with a size close to 4 nm are found on the Au core. They form a loose particle shell (Figure 3A). After 6 min, the shells become much more dense. We suggest that the collision and fusion of small Cu₂O particles with loosely coated Au NRs result in thickening and densification of the shell (Figure 3B). At 25 min, the formation of the dense shell is finished (Figure 3C). On the basis of the above observations, the formation of Au@Cu₂O may be described as follows: After NaOH is added to the growth solution, cupric hydroxides form both in the solution and on the Au core. The growth solution becomes turbid. After ascorbic acid (AA) is added, cupric hydroxides are reduced to small Cu₂O particles. The growth solution becomes clear, indicating the formation of much smaller particles. Small Cu₂O particles grow via aggregation and fusion, eventually giving rise to a dense shell. A schematic illustration of the growth mechanism for the Au@Cu₂O core–shell structure is shown in Figure 3F.

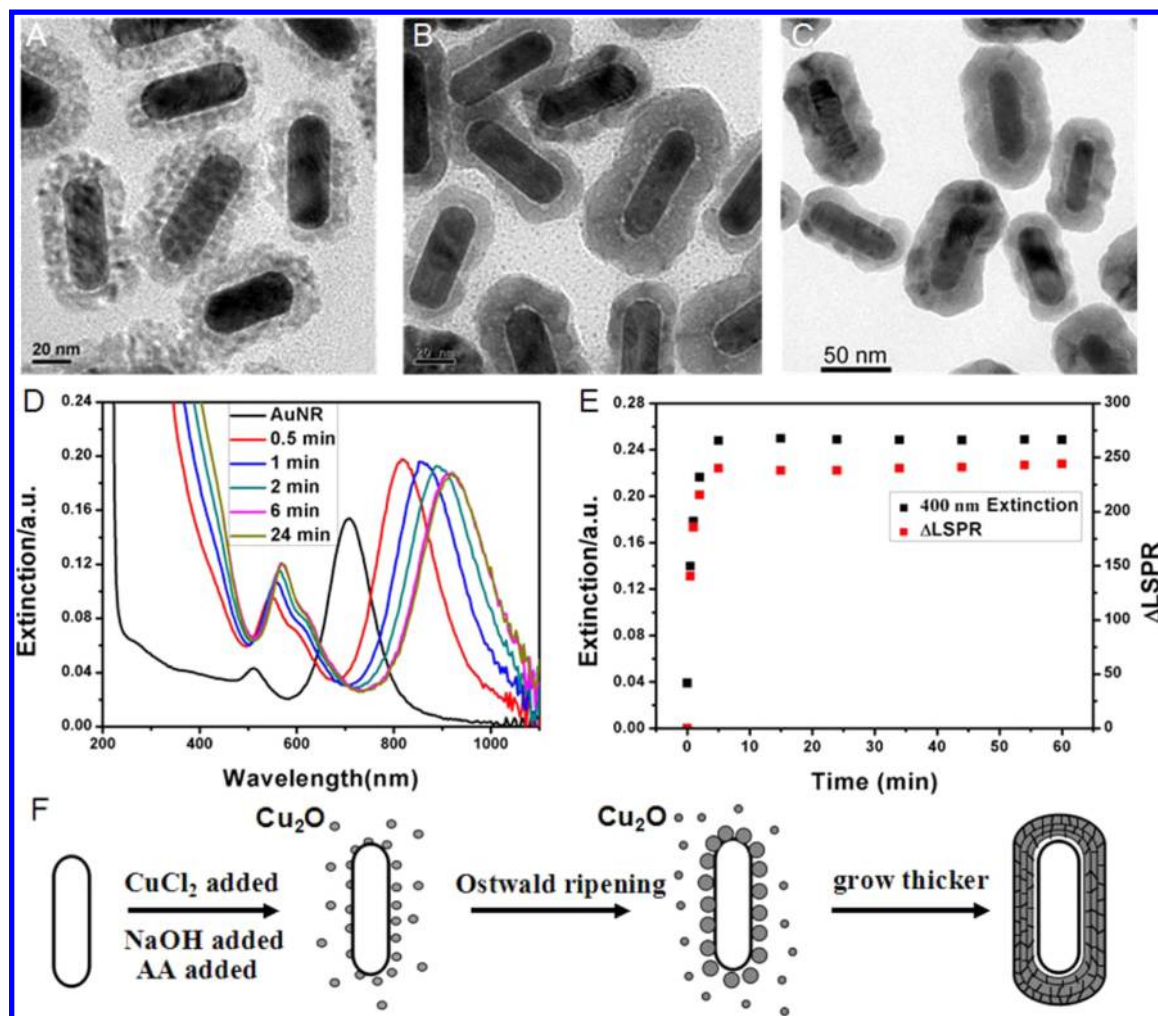


Figure 3. TEM images of the products collected after adding AA for (A) 2, (B) 6, and (C) 25 min. (D) Longitudinal SPR peak shift vs growth time during shell formation. (E) Ext_{400 nm} intensity and LSPR shift vs growth time during shell formation. (F) Schematic illustration of Cu₂O shell formation on Au 710 rod via aggregation and fusion.

Our strategy provides a simple way to fine tune the shell in a relative thin thickness range while maintaining the symmetry and overall morphology of the core particle. At a fixed concentration of Cu²⁺, a varying Au NR concentration is used to achieve different shell thicknesses. Figure 4 shows extinction spectra, TEM images, and suspension photographs of four Au@Cu₂O samples with different shell thicknesses. As shown in Figure S4, distribution histograms of the shell thickness indicate that the relative standard deviation is between 21 and 11%. The shell thickness increases by decreasing the volume of the Au seed. Theoretically, the thickness can be further reduced by increasing the concentration of the Au seeds. However, when the concentration of the Au nanorod is increased to 500 pM, the Cu₂O shell is incomplete because of fewer available Cu₂O NPs per rod (Figure S5). However, if we lower the rod concentration to 75 pM, a large number of pure Cu₂O NPs are found. This substantiates that the binding of small Cu₂O NPs on the rod surface is competitive with their self-aggregation: at low rod concentration, the self-aggregation of small Cu₂O NPs dominates.²⁴ In the absence of Au NRs, we can obtain pure Cu₂O NPs. The band gap of obtained Cu₂O NPs is 1.99 eV, similar to the bulk value (Figure S6). In contrast, the band gap of the Cu₂O shell for the four core–shell structures is ~2.36 eV (Figure S7).

Effects of the Cu₂O Shell on the SPR Features of the Au Core.

As-prepared Au@Cu₂O displays interesting spectral features in the visible and near-infrared spectral range. It can be roughly divided into two parts (Figure 4A). The strong absorbance at wavelength shorter than 500 nm is dominated by the interband transition of the Cu₂O shell with three exciton peaks at 225, 283, and 383 nm.²⁵ With decreasing thickness of the Cu₂O shell, the color of the suspension changes from blue-green to dark green to emerald green. The spectral features on the red side of 500 nm reflect the impact of the shell on the localized SPR of the Au nanorod. Because of the large refractive index of Cu₂O, both longitudinal and transverse SPR bands are red shifted. At a shell thickness of 11.6 nm, the longitudinal SPR shifts 160 nm from 640 to 806 nm. For the transverse SPR, a 60 nm red shift is observed. However, the transverse SPR band is obviously broadened, suggesting the appearance of a new resonance feature. To understand this observation better, FDTD is used to simulate the extinction features of the nanostructure. The shape of the sample is assumed to be a cylinder in the middle and two semiellipsoids at the two ends (Scheme S1). The geometric parameters of the Au core and Cu₂O shell are given in Table S2 in the Supporting Information. The refractive indexes of Au and Cu₂O are from Johnson Christy and the Palik database, respectively.²⁶ The

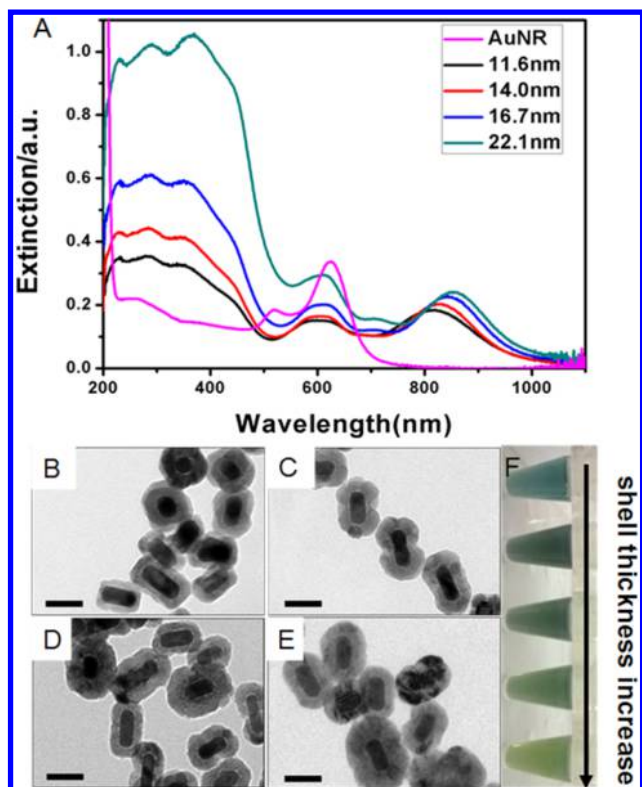


Figure 4. (A) Extinction spectra of the Au nanorod and Au@Cu₂O nanostructures dispersed in water. TEM images of Au@Cu₂O nanostructures with shell thicknesses of (B) 11.6, (C) 14.0, (D) 16.7, and (E) 22.1 nm, respectively. Scale bar: 50 nm. (F) Photograph of colloidal suspensions of the Au nanorod and Au@Cu₂O nanostructures.

refractive index of the surrounding is set to be 1.33 for H₂O because the samples are dispersed in water. From the TEM image (Figure 1A), there seems to be a gap between the Au NR and the Cu₂O shell. We postulate that during the formation of a compact shell the Cu₂O nanocrystallites originally attached to the core may move outward to match the neighboring nanocrystallites better. Such movement may leave a gap between the core and the shell. By simulation without a gap, we found that the simulated peaks deviate greatly from the experimental spectra (Figure S8A and Figure 5B). By assuming a 1 nm gap with a refractive index of 1.33, the simulated results match the experimental spectra much better (Figure 5A,C). Upon transverse excitation as shown in Figure 5C, the calculation results show that this region is composed of two transverse excitation modes. From the near-field patterns (Figure 5D,E), the longer-wavelength band looks like a dipolar resonance, similar to the transverse dipole of a pure Au rod (Figure S1B). In contrast, the shorter-wavelength band seems to be an octupolar resonance. Surface charge pattern analysis further proves that these two resonances are dipolar and octupolar dominant, respectively. (Figure 5F,G). We term them as D (dipolar) and O (octupolar), respectively. In the case of no gap between the core and the shell, these two modes are well-separated bands and the octupolar mode is stronger than the dipolar mode. At a fixed core diameter of 24 nm, the intensity of both modes is enhanced by increasing AR, which can be ascribed to the enlarged overall size. Furthermore, the relative intensity of the octupolar mode increases with respect to that of the dipolar mode by increasing AR from 2 to 3. It is

noted that the octupolar mode cannot be observed at smaller ARs, such as AR = 1.5 and 1 (Figure S9A). At a fixed core volume, again the octupolar mode appears at higher ARs (Figure S9B). Indeed, by changing the core from a rod to a sphere with the same core volume, the octupolar mode is not observed (Figure S10). Therefore, at the same volume, large AR aids the generation of multipolar resonance. This is verified experimentally in Figure 3D. When we use the Au core with a larger AR, the octupolar mode dominates. The spectral features between 500 and 700 nm are caused by the high refractive of Cu₂O rather than plasmon splitting as a result of plasmon-exciton coupling. To further confirm this, we calculated the extinction spectra of the Au NR by using a dielectric shell ($\epsilon = 7.3$). Extinction spectra similar to those in Figure 5A are obtained (Figure S9C). If we change Cu₂O to Si₂O ($\epsilon = 1.45$), then there is only one transverse mode in the spectrum (Figure S9C). These results suggest that it is the high refractive and anisotropic geometry of Au NR that causes the redistribution of charges and the generation of multipolar resonances.

For absorbance, Cu₂O coating enhances the TSPR absorbance and slightly weakens the LSPR absorbance with respect to the Au nanorod. Moreover, coating leads to a greater reduction in the scattering intensity of the LSPR mode with respect to the Au nanorod owing to the effective screening of the electric field of the Au nanorod by the Cu₂O shell (Figure S11).²⁷ The high dielectric function ($\epsilon = 7.3$) of the Cu₂O shell reduces the penetration depth of the localized surface plasmon field of the Au core into the medium. Again, because of the anisotropic geometry of the Au nanorod, the responses of LSPR and TSPR to the Cu₂O coating are different. For the LSPR mode, the scattering intensity of the Au core is strong (Figure S11A). After Cu₂O is coated, decreased core scattering owing to the shell screening effect is larger than the increased Mie scattering resulting from the overall size enlargement. This leads to a decrease in total scattering for the LSPR mode of the core-shell rod (Figure S11A) compared to that of the Au core. Thus, upon LSPR excitation, the Au@Cu₂O nanorod offers a better photothermal effect than does the pure Au nanorod. For the bare Au nanorod, the absorption/extinction (Abs/Ext) ratio is ~85% upon exciting the LSPR band. After coating with Cu₂O, the ratio increases to above 90% (Figure 5B). In contrast, for the TSPR mode, the scattering intensity of the Au core is very weak (Figure S11B). The Cu₂O coating further decreases its contribution. The Mie scattering of the Cu₂O shell dominates the TSPR scattering for Au NR@Cu₂O (Figure S11B). Therefore, the TSPR scattering intensity of Au NR@Cu₂O is larger than that of the Au NR core. For the Au nanosphere with the same core volume of $V_{\text{core}} = 19\,292\text{ nm}^3$, because of very low core scattering, the Mie scattering of the Cu₂O shell dominates (Figure S10B). Thus, the scattering intensity of Au NS@Cu₂O is larger than that of the Au core, which is similar to the transverse SPR mode of the gold nanorod.

Probing Defect States upon LSPR Excitation. We found that dissolved O₂ is able to induce the oxidation of the Cu₂O shell. The generation of Cu²⁺ and its dissolution from the rod surface cause the spectrum change (Figure S12A). Increasing temperature accelerates the shell degradation (Figure S12B). After the removal of dissolved oxygen by degassing the sample solution with N₂, no changes in extinction spectra are observed (Figure S13). We monitor the photostability of the Cu₂O shell by measuring the LSPR blue shift upon laser irradiation. Because of the photothermal effect, the sample solution is

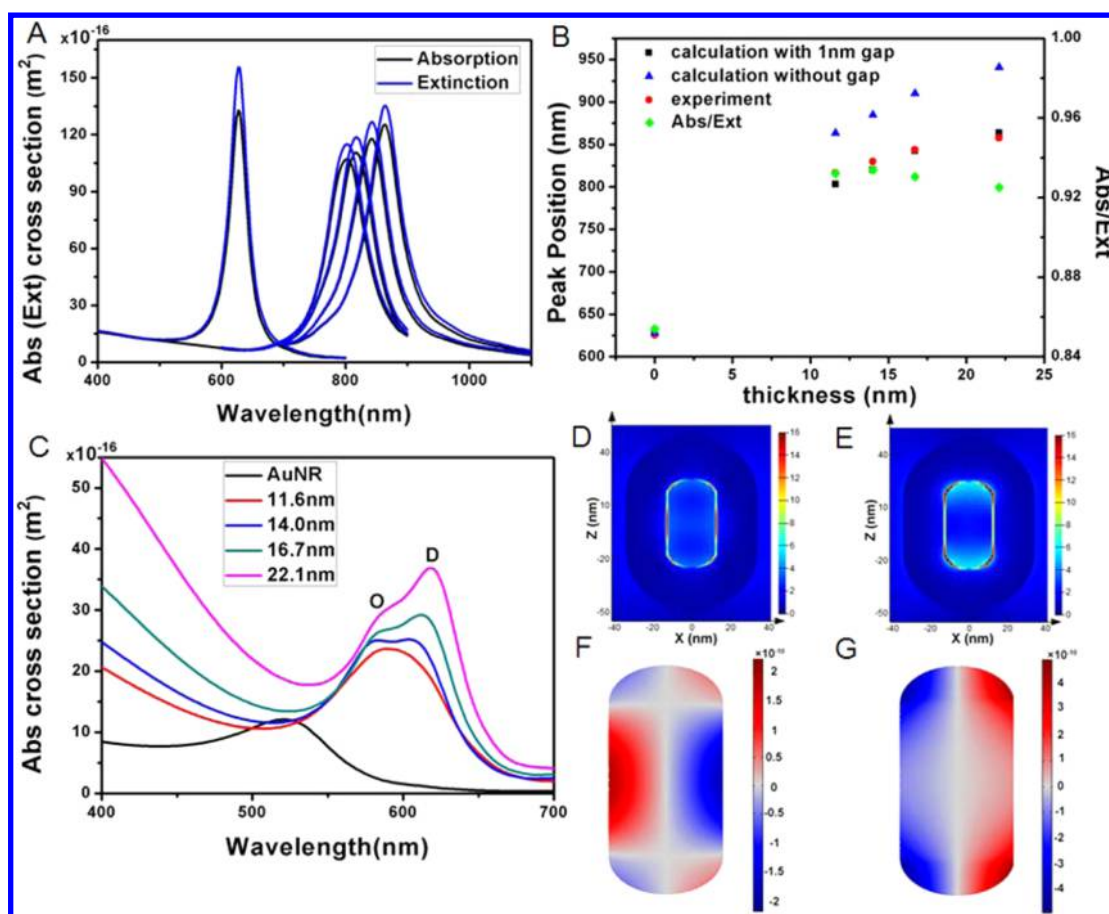


Figure 5. (A) Calculated SPR spectra upon longitudinal excitation at different shell thicknesses. (B) Longitudinal SPR peak position and Abs/Ext ratio vs shell thickness. (C) Calculated SPR spectra upon transverse excitation at different shell thickness. (D, E) Electromagnetic fields of Au@Cu₂O-4 at 589 and 618 nm, respectively. The color scale bar shows the relative increase in field enhancement $|E|^2/|E_0|^2$. (F, G) Corresponding charge patterns at 589 and 618 nm on the Au NR surface, respectively.

heated. To exclude the impact of the thermal effect, the heating and cooling curves of the four samples were first measured using a 808 nm laser (Figure 6A). Initially, the temperature of the sample solutions increases quickly. It reaches equilibrium at ca. 10 min. Because of slight differences in the absorbance coefficient at 808 nm, the thicker shell achieves a slightly higher temperature. The highest temperatures are all below 50 °C. Therefore, we use the 50 °C heating experiment to evaluate the thermal effect. The relative volume variations of the shell after 30 min of water-bath heating are used to reflect the density of defect states in the shell whereas those after 30 min of laser irradiation are used to evaluate the LSPR-mediated enhancement. It is found that thicker shells have higher thermal stabilities (Figure 6B). We suggest that a thicker shell has a low density of defect states. This agrees with the results of Mahmoud.³ They found a long exciton lifetime for a thick Cu₂O shell. Therefore, shell degradation is related to the density of defect states. Upon laser irradiation, the shell degradation is aggravated. A thin shell degrades more severely than does a thick shell. For an 11.6 nm shell, the photoinduced degradation is 22.0%, whereas it is reduced to 8.5% for a 22.1 nm shell. Such a difference hints at the involvement of LSPR-mediated effects.

In our case, direct hot electron injection from plasmonic NPs into the semiconductor can be ignored.²⁸ The Fermi energy of Au is −5.1 eV, and the conducting band edge for Cu₂O is −3.2 eV.^{29,30} The photon energy of the 808 nm laser is around 1.58 eV, and the excited hot electrons do not have sufficient energy

to enter the conduction band (CB) of the Cu₂O shell. It has been reported that there are copper vacancies and oxygen interstitials in Cu₂O, and the former is the dominant defect.³¹ These vacancies and interstitials lead to a cation deficiency that would bind electrons and form the so-called trap states. Previous studies suggested that the electron transition related to the copper vacancies produces photoluminescence at about 900–1050 nm.^{32,33} Therefore, the copper-vacancy-related transition overlaps with the 808 nm laser and is able to be enhanced by localized SPR effects.

To evaluate the field enhancement, we calculated the local electromagnetic field at 808 nm using FDTD simulation (Figure 6C,D). As expected, $|E|^2/|E_0|^2$ decays exponentially with increasing shell thickness. Also we found that the relative variation in volume exhibits an exponential decay with shell thickness. If we normalize the decay curves, we find that the calculated field decay is much steeper than the relative variation in the volume decays (Figure 6E). To gain more insight into the localized electromagnetic field (LEF) enhancement, we further measured SERS of 4-MPy molecules. As shown in Figure S14 and Table S3, the SERS intensity of 4-MPy also exhibits an exponential decay with shell thickness. The decay of EF values versus shell thickness is, however, smaller than the calculated EF decay curve. This indicates that the experimental enhancement factor (EF) values do not reach the theoretical values. It is logical that the size and shape distributions discount the field enhancement. Because SERS is proportional to the

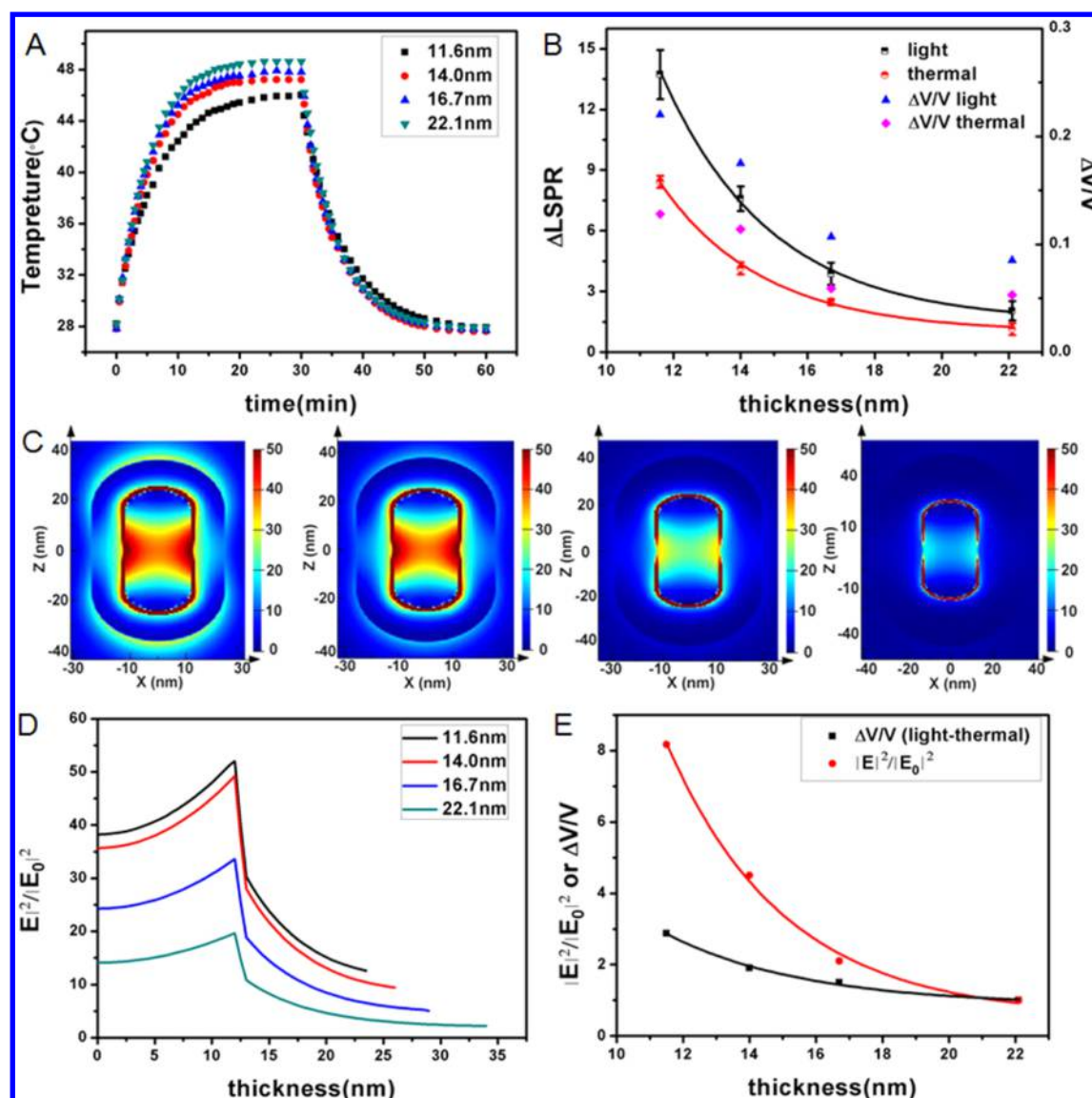


Figure 6. Photodegradation of Au@Cu₂O nanostructures upon longitudinal SPR excitation and possible mechanism. (A) Temperature rising and cooling curves. (B) LSPR peak shift upon photo and thermal degradation (left axis) and relative volume variation after subtracting the thermal effect (right axis). (C) Electromagnetic field at 808 nm (the shell thickness increases from left to right). The color scale bar shows the relative increase in field enhancement $|E|^2/|E_0|^2$. (D) Electric field intensity profiles along the length axis from the center of the nanorod. (E) Normalized relative volume variation and $|E|^2/|E_0|^2$ vs shell thickness.

$E^4/|E_0|^4$, the similar decay patterns for SERS and photodegradation mean that the nonradiative RET process contributes to an extra enhancement for photodegradation. This kind of energy transfer does not require direct contact and can reach further than charge transfer.¹² The localized SPR-mediated effects are schematically shown in Figure 7.

CONCLUSIONS

To utilize localized surface-plasmon-enhanced effects, Au@Cu₂O core-shell particles with relatively thin shells are prepared. Cupric hydroxides are reduced to Cu₂O nuclei upon adding ascorbic acid. Aggregation and fusion of small Cu₂O nanoparticles on Au rods result in the formation of dense Cu₂O shells. For thin shells, the NIR extinction spectra are dominated by the localized SPR features of the Au NR but are modified by Cu₂O greatly. Octupolar resonances are observed experimentally and verified by theoretical simulations. In

comparison to gold nanospheres, anisotropic AuNPs can hold multipolar resonance at smaller sizes. The existence of defect states in the shell causes shell degradation. Resonant plasmon excitation aggravates defect-mediated photodegradation. The tunable plasmon resonance of the core makes the selective excitation of specific states possible. It provides a unique way to probe and distinguish defect states.

EXPERIMENTAL SECTION

Materials. Sodium borohydride (NaBH₄), chlorauric acid (HAuCl₄·3H₂O), cetyltrimethylammonium bromide (CTAB), ascorbic acid (AA), and silver nitrate (AgNO₃) were purchased from Alfa Aesar and used as received. 4-Mercaptopyridine (4-Mpy, 96%) was purchased from Acros Organics and used without any further purification. Sodium hydroxide (NaOH), copper(II) chloride dihydrate (CuCl₂·2H₂O), and anhydrous ethanol were at least analytical reagent grade and purchased from Beijing Chemical Reagent

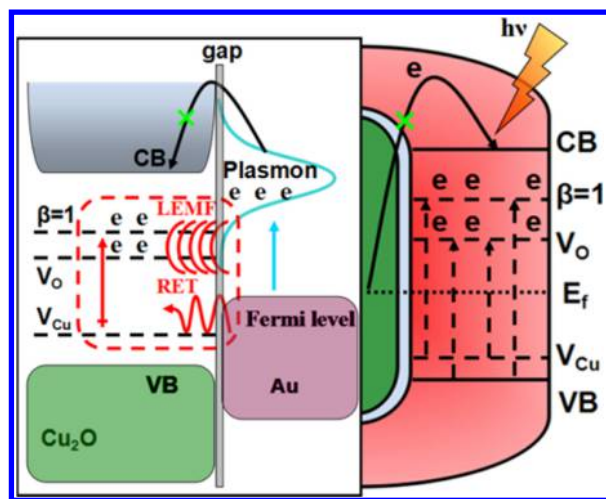


Figure 7. Shell photodegradation mechanism by various SPR-induced enhancement effects in the Au@Cu₂O core-shell structure ($\beta = 1$ means V_{Cu} β -state). The defect-state levels are adopted from ref 31.

Company (Beijing, China). Milli-Q water (18 M Ω cm) was used for all solution preparations.

Synthesis of Au NRs. Au NRs were synthesized using a well-developed seed-mediated growth method.³⁴ Au NRs with an LSPR maximum at 710 nm (Au710) were used to investigate the growth of the Cu₂O shell, and Au640 was used to study LSPR-mediated effects.

Briefly, CTAB-capped Au seeds were synthesized by the chemical reduction of HAuCl₄ with NaBH₄: CTAB (7.5 mL, 0.1 M) was mixed with HAuCl₄ (100 μ L, 24 mM) and diluted with water to 9.4 mL. Then ice-cold NaBH₄ (0.6 mL, 10 mM) was added with magnetic stirring. The Au seeds were used within 2–5 h.

Au710 nm was synthesized via adding AA three times.^{35,36} A seed solution (0.12 mL) was added to the growth solution consisting of CTAB (100 mL, 0.1 M), HAuCl₄ (2.04 mL, 24 mM), AgNO₃ (1.05 mL, 0.01M), and AA (0.1 M, 0.552 mL). After 12 h, two injections of AA (0.1 M, 0.552 mL) were performed with stirring over a 40 min interval. The growth temperature was kept at 30 $^{\circ}$ C. After 12 h, the Au NRs were purified by centrifugation (12 000 rpm, 5 min) once and dispersed in deionized water.

Au640 nm was synthesized in the presence of H₂SO₄.³⁷ The growth solution was a mixture of CTAB (100 mL, 0.1 M), HAuCl₄ (2.05 mL, 24.7 mM), AgNO₃ (0.45 mL, 0.01 M), H₂SO₄ (2.0 mL, 0.5 M), and AA (0.8 mL, 0.1 M). A Au seed solution (240 μ L) was added. The growth was kept at 30 $^{\circ}$ C for 12 h. Then, the Au NRs were purified by centrifugation (12 000 rpm, 5 min) once and dispersed in deionized water.

Synthesis of Au@Cu₂O with Different Shell Thicknesses and Cu₂O Nanoparticles. The Cu₂O shell thickness is tuned by varying the concentration of the Au NRs. Four volumes of Au NRs suspensions (6, 4.5, 3, and 1.5 mL) were centrifuged. Each precipitate was dispersed with 1 mL of CTAB solution (0.1 M) to obtain different concentrations of Au NRs (corresponding to 400, 300, 200, and 100 pM particle concentrations, respectively). Each Au NRs suspension was first diluted with 1.842 mL of deionized water. Then, 30 μ L of 0.1 M CuCl₂ and 37.5 μ L of 0.6 M NaOH were added sequentially. In the end, 90 μ L of AA (0.1M) was added. The reaction volume is \sim 3 mL. The mixtures were left undisturbed for 25 min in a 30 $^{\circ}$ C water bath. The order of addition of NaOH and AA is found to be important. If we add AA first and then NaOH, then nanostructures with poor morphology are obtained (Figure S3). After reaction, the product was purified by centrifugation (8000 rpm, 3 min) and washed with deionized water and anhydrous ethanol several times. The precipitate was then dispersed in either deionized water or anhydrous ethanol. The zeta potentials of the purified samples dispersed in ethanol are ca. -30 mV. With increasing shell thickness, the four samples are labeled as Au@Cu₂O-1, Au@Cu₂O-2, Au@Cu₂O-3, and Au@Cu₂O-4,

respectively. And the side-facet thickness of the Cu₂O shell is used to represent the shell thickness herein.

Pure Cu₂O nanoparticles were obtained in the absence of Au NRs. Cu₂O nuclei grow large via coalescence.

Theoretical Simulation. The localized SPR bands were obtained and electric field enhancements of the Au nanorod and the Au@Cu₂O structure were performed using FDTD Solutions 8.6 developed by Lumerical Solutions, Inc. During the simulations, an electromagnetic pulse with a different wavelength range was launched in a box containing a target nanostructure, and the mesh was set to be 0.5 nm. The charge pattern was simulated by COMSOL Multiphysics. The detailed parameters of the Au nanorod and Au@Cu₂O are given in the Supporting Information, Table S1.

Measurement of the Increasing Temperature and Cooling Curves. The sample solutions were prepared by adding 300 μ L of nanoparticles (0.45 nM) to 1.5 mL of deionized water. They were then irradiated with an 808 nm laser at room temperature for 30 min and cooled by switching off the laser. The solution temperature was monitored with a thermocouple connected to a digital thermometer.

Degradation of the Nanostructures. The degradation of the Au@Cu₂O core-shell structure was monitored by the blue shift in LSPR under 808 nm laser irradiation or water bath heating. The degradation is evaluated using the relative volume variation of the shell by first converting the LSPR peak wavelength to shell thickness using experimental data (LSPR peak (nm) = (872.12 $-$ 246.52) \times exp(1/7.776), $R^2 = 0.9995$, l is shell thickness (nm)) and then converting the shell thickness to a shell volume. The sample solution was prepared by combining 300 μ L of 0.45 nM nanoparticles with 1.5 mL of deionized water. Each nanoparticle sample was divided into two parts. One part was put in a 50 $^{\circ}$ C water bath to study the thermal degradation; the other part was irradiated with a laser to investigate photodegradation. The extinction spectra were recorded after 30 min in a water bath or photoirradiation. The laser power was 1.145 W as measured by a laser power meter. The samples were naturally cooled to room temperature before their extinction spectra were recorded.

Raman Experiments. 4-Mpy molecules were adsorbed onto the Au@Cu₂O nanoparticles or Au nanorod by the following procedure: the above samples were dispersed in different amounts of deionized water, and the concentration of the Au core was adjusted to be \sim 1.0 nM. Then, 4-Mpy was added to Au@Cu₂O or Au nanorod suspensions. The concentration of 4-Mpy is 5 μ M. The mixtures were undisturbed for 3 h to guarantee the adsorption equilibrium. To record the Raman spectra, the samples were added to a PDMS mold for Raman measurements.

Characterization. X-ray diffraction data were collected with a D/MAX-TTRIII (CBO) diffractometer. UV-vis-NIR extinction spectra were obtained with a Varian Cary 50. XPS spectra were collected using an ESCALAB250Xi system. Transmission electron microscopy (TEM) measurements were performed on a TECNAI G² 20 S-TWIN at an accelerating voltage of 200 kV. High-resolution transmission electron microscopy (HRTEM) images were captured on a FEI TECNAI G² F20 U-TWIN at an accelerating voltage of 200 kV. Raman spectra were obtained with a confocal micro-Raman spectrometer (Renishaw inVia Plus) through a 50 \times objective lens. The 785 nm laser was used as the source of excitation. The enhanced Raman spectra of 4-Mpy adsorbed on Au@Cu₂O or the Au nanorod were acquired with 30 and 10 s of exposure time, respectively. A diode laser at 808 nm (GCSLS-05-7W00) from Daheng Optics was employed for photothermal degradation.

■ ASSOCIATED CONTENT

● Supporting Information

Additional results of structure analysis, calculations, and SERS activity tests of the samples. This material is available free of charge via the Internet at <http://pubs.acs.org>.

■ AUTHOR INFORMATION

Corresponding Authors

*E-mail: msong@csu.edu.cn.

*E-mail: huzj@nanocr.cn.

*E-mail: wuxc@nanocr.cn.

Notes

The authors declare no competing financial interest.

ACKNOWLEDGMENTS

This work was supported by the National Key Basic Research Program of China (2012CB934001 and 2011CB932802) and the National Natural Science Foundation of China (grant nos. 91127013, 21173056, and 11304054).

REFERENCES

- (1) Li, J. H.; Zhang, J. Z. Optical properties and applications of hybrid semiconductor nanomaterials. *Coord. Chem. Rev.* **2009**, *253*, 3015–3041.
- (2) Liu, S. W.; Yu, J. G.; Jaroniec, M. Tunable Photocatalytic Selectivity of Hollow TiO₂ Microspheres Composed of Anatase Polyhedra with Exposed {001} Facets. *J. Am. Chem. Soc.* **2010**, *132*, 11914–11916.
- (3) McLaren, A.; Valdes-Solis, T.; Li, G. Q.; Tsang, S. C. Shape and Size Effects of ZnO Nanocrystals on Photocatalytic Activity. *J. Am. Chem. Soc.* **2009**, *131*, 12540–12541.
- (4) Youngblood, W. J.; Lee, S. H. A.; Maeda, K.; Mallouk, T. E. Visible Light Water Splitting Using Dye-Sensitized Oxide Semiconductors. *Acc. Chem. Res.* **2009**, *42*, 1966–1973.
- (5) Wang, B.; Kerr, L. L. Stability of CdS-coated TiO₂ solar cells. *J. Solid State Electrochem.* **2012**, *16*, 1091–1097.
- (6) Mahmoud, M. A.; Qian, W.; El-Sayed, M. A. Following Charge Separation on the Nanoscale in Cu₂O-Au Nanoframe Hollow Nanoparticles. *Nano Lett.* **2011**, *11*, 3285–3289.
- (7) DuChene, J. S.; Sweeny, B. C.; Johnston-Peck, A. C.; Su, D.; Stach, E. A.; Wei, W. D. Prolonged Hot Electron Dynamics in Plasmonic-Metal/Semiconductor Heterostructures with Implications for Solar Photocatalysis. *Angew. Chem., Int. Ed.* **2014**, *53*, 7887–7891.
- (8) Xiao, M. D.; Jiang, R. B.; Wang, F.; Fang, C. H.; Wang, J. F.; Yu, J. C. Plasmon-enhanced chemical reactions. *J. Mater. Chem. A* **2013**, *1*, 5790–5805.
- (9) Ingram, D. B.; Linic, S. Water Splitting on Composite Plasmonic-Metal/Semiconductor Photoelectrodes: Evidence for Selective Plasmon-Induced Formation of Charge Carriers near the Semiconductor Surface. *J. Am. Chem. Soc.* **2011**, *133*, 5202–5205.
- (10) Liu, Z.; Hou, W.; Pavaskar, P.; Aykol, M.; Cronin, S. B. Plasmon Resonant Enhancement of Photocatalytic Water Splitting Under Visible Illumination. *Nano Lett.* **2011**, *11*, 1111–1116.
- (11) Kumar, M. K.; Krishnamoorthy, S.; Tan, L. K.; Chiam, S. Y.; Tripathy, S.; Gao, H. Field Effects in Plasmonic Photocatalyst by Precise SiO₂ Thickness Control Using Atomic Layer Deposition. *ACS Catal.* **2011**, *1*, 300–308.
- (12) Cushing, S. K.; Li, J. T.; Meng, F.; Senty, T. R.; Suri, S.; Zhi, M. J.; Li, M.; Bristow, A. D.; Wu, N. Q. Photocatalytic Activity Enhanced by Plasmonic Resonant Energy Transfer from Metal to Semiconductor. *J. Am. Chem. Soc.* **2012**, *134*, 15033–15041.
- (13) Fernando, C. A. N.; de Silva, P. H. C.; Wethasinha, S. K.; Dharmadasa, I. M.; Delsol, T.; Simmonds, M. C. Investigation of n-type Cu₂O layers prepared by a low cost chemical method for use in photo-voltaic thin film solar cells. *Renewable Energy* **2002**, *26*, 521–529.
- (14) Huang, W. C.; Lyu, L. M.; Yang, Y. C.; Huang, M. H. Synthesis of Cu₂O Nanocrystals from Cubic to Rhombic Dodecahedral Structures and Their Comparative Photocatalytic Activity. *J. Am. Chem. Soc.* **2012**, *134*, 1261–1267.
- (15) Zhang, L.; Blom, D. A.; Wang, H. Au-Cu₂O Core-Shell Nanoparticles: A Hybrid Metal-Semiconductor Heteronanostructure with Geometrically Tunable Optical Properties. *Chem. Mater.* **2011**, *23*, 4587–4598.
- (16) Zhang, L.; Jing, H.; Boisvert, G.; He, J. Z.; Wang, H. Geometry Control and Optical Tunability of Metal-Cuprous Oxide Core-Shell Nanoparticles. *ACS Nano* **2012**, *6*, 3514–3527.
- (17) Liu, D. Y.; Ding, S. Y.; Lin, H. X.; Liu, B. J.; Ye, Z. Z.; Fan, F. R.; Ren, B.; Tian, Z. Q. Distinctive Enhanced and Tunable Plasmon Resonant Absorption from Controllable Au@Cu₂O Nanoparticles: Experimental and Theoretical Modeling. *J. Phys. Chem. C* **2012**, *116*, 4477–4483.
- (18) Kuo, C. H.; Hua, T. E.; Huang, M. H. Au Nanocrystal-Directed Growth of Au-Cu₂O Core-Shell Heterostructures with Precise Morphological Control. *J. Am. Chem. Soc.* **2009**, *131*, 17871–17878.
- (19) Kong, L. N.; Chen, W.; Ma, D. K.; Yang, Y.; Liu, S. S.; Huang, S. M. Size control of Au@Cu₂O octahedra for excellent photocatalytic performance. *J. Mater. Chem.* **2012**, *22*, 719–724.
- (20) Wang, W. C.; Lyu, L. M.; Huang, M. H. Investigation of the Effects of Polyhedral Gold Nanocrystal Morphology and Facets on the Formation of Au–Cu₂O Core–Shell Heterostructures. *Chem. Mater.* **2011**, *23*, 2677–2684.
- (21) Fan, F. R.; Liu, D. Y.; Wu, Y. F.; Duan, S.; Xie, Z. X.; Jiang, Z. Y.; Tian, Z. Q. Epitaxial Growth of Heterogeneous Metal Nanocrystals: From Gold Nano-octahedra to Palladium and Silver Nanocubes. *J. Am. Chem. Soc.* **2008**, *130*, 6949–6951.
- (22) Wu, C. K.; Yin, M.; O'Brien, S.; Koberstein, J. T. Quantitative Analysis of Copper Oxide Nanoparticle Composition and Structure by X-ray Photoelectron Spectroscopy. *Chem. Mater.* **2006**, *18*, 6054–6058.
- (23) Toupin, M.; Brousse, T.; Bélanger, D. Charge Storage Mechanism of MnO₂ Electrode Used in Aqueous Electrochemical Capacitor. *Chem. Mater.* **2004**, *16*, 3184–3190.
- (24) Sun, H.; He, J. T.; Wang, J. Y.; Zhang, S. Y.; Liu, C. C.; Sritharan, T.; Mhaisalkar, S.; Han, M. Y.; Wang, D.; Chen, H. Y. Investigating the Multiple Roles of Polyvinylpyrrolidone for a General Methodology of Oxide Encapsulation. *J. Am. Chem. Soc.* **2013**, *135*, 9099–9110.
- (25) Qiu, C.; Zhang, L.; Wang, H.; Jiang, C. Y. Surface-Enhanced Raman Scattering on Hierarchical Porous Cuprous Oxide Nanostructures in Nanoshell and Thin-Film Geometries. *J. Phys. Chem. Lett.* **2012**, *3*, 651–657.
- (26) Gold: Johnson, P. B.; Christy, R. W. *Phys. Rev. B: Condens. Matter Mater. Phys.* **1972**, *6*, 4370–4379. Cu₂O: *Handbook of Optical Constants of Solids II*; Palik, E. D., Ed.; Academic Press: Waltham, MA, 1991.
- (27) Barnes, W. L. Surface Plasmon-polariton length scales: a route to sub-wavelength optics. *J. Opt. A: Pure Appl. Opt.* **2008**, *8*, s87–s93.
- (28) Knight, M. W.; Sobhani, H.; Nordlander, P.; Halas, N. J. Photodetection with Active Optical Antennas. *Science* **2011**, *332*, 702–704.
- (29) Horiguchi, Y.; Kanda, T.; Torigoe, K.; Sakai, H.; Abe, M. Preparation of Gold/Silver/Titania Trilayered Nanorods and Their Photocatalytic Activities. *Langmuir* **2014**, *30*, 922–928.
- (30) Hsueh, T. J.; Hsu, C. L.; Chang, S. J.; Guo, P. W.; Hsieh, J. H.; Chen, I. C. Cu₂O/n-ZnO nanowire solar cells on ZnO:Ga/glass templates. *Scr. Mater.* **2007**, *57*, 53–56.
- (31) Raebiger, H.; Lany, S.; Zunger, A. Origins of the p-type nature and cation deficiency in Cu₂O and related materials. *Phys. Rev. B* **2007**, *76*, 045209.
- (32) Chowdhury, A.; Bijalwana, P. K.; Sahu, R. K. Investigations on the role of alkali to obtain modulated defect concentrations for Cu₂O thin films. *Appl. Surf. Sci.* **2014**, *289*, 430–436.
- (33) Shi, H.; Yu, K.; Sun, F.; Zhu, Z. Q. Controllable synthesis of novel Cu₂O micro/nano-crystals and their photoluminescence, photocatalytic and field emission properties. *CrystEngComm* **2012**, *14*, 278–285.
- (34) Nikoobakht, B.; El-Sayed, M. A. Preparation and Growth Mechanism of Gold Nanorods (NRs) Using Seed-Mediated Growth Method. *Chem. Mater.* **2003**, *15*, 1957.
- (35) Khanal, B. P.; Zubarev, E. R. Polymer-Functionalized Platinum-On-Gold Bimetallic Nanorods. *Angew. Chem., Int. Ed.* **2009**, *48*, 6888–6891.

(36) Alvarez-Puebla, R.; Agarwal, A.; Manna, P.; Khanal, B. P.; Aldeanueva-Potel, P.; Carbo-Argibay, E.; Pazos-Perez, N.; Vigderman, L.; Zubarev, E. R.; Kotov, N. A.; Liz-Marzan, L. M. Gold nanorods 3D-supercrystals as surface enhanced Raman scattering spectroscopy substrates for the rapid detection of scrambled prions. *Proc. Natl. Acad. Sci. U.S.A.* **2011**, *108*, 8157–8161.

(37) Liu, M. Z.; Guyot-Sionnest, P. Mechanism of silver(I)-assisted growth of gold nanorods and bipyramids. *J. Phys. Chem. B* **2005**, *109*, 22191–22200.